The GLASS Land Surface Temperature Product

Ji Zhou ⑩, *Member, IEEE*, Shunlin Liang ⑩, *Fellow, IEEE*, Jie Cheng, *Member, IEEE*,
Yujia Wang, and Jin Ma, *Student Member, IEEE*

Abstract—Land surface temperature (LST) is one of the most important geophysical parameters at the earth's surface. Satellite LST products are beneficial for scientific communities with a variety of applications. The Global Land Surface Satellite (GLASS) LST product has been generated for 1983, 1993, 2003, and 2013 from historical NOAA-7 and NOAA-14 AVHRR data and recent Terra/Aqua MODIS data. The spatial resolution of the instantaneous GLASS LST product is 0.05° for 1983 and 1993 and is 1 km for 2003 and 2013. The algorithm for generating the GLASS LST product is based on a multialgorithm ensemble approach, which combines nine split-window algorithms with good performance in training, testing, and sensitivity analysis. The validation results based on *in situ* measurements demonstrate that the GLASS-AVHRR LST product has an accuracy of 2.89 K at Barrow site; the GLASS-MODIS LST product has an accuracy of 1.82–2.15 K at six grassland/cropland SURFRAD sites at nighttime, which is a similar accuracy to the official MODIS LST product. Systematic underestimation of LST at Desert Rock, NV (arid shrubland) has been found and has been attributed to uncertainties associated with land surface emissivities and other input datasets. Further intercomparison indicates that the GLASS-MODIS LST product agrees well with the official MODIS LST, with mean bias deviations/root mean square deviations of –1.19 K/1.87 K and 1.89 K/2.27 K for the two granules under examination. Nevertheless, the validation of the GLASS LST product is currently in a preliminary stage, and more in-depth examinations are still needed.

Index Terms—Global Land Surface Satellite (GLASS), land surface temperature (LST), National Oceanic and Atmospheric Administration (NOAA) AHVRR, split-window algorithm, Terra/Aqua MODIS.

I. INTRODUCTION

LAND surface temperature (LST) is one of the most important geophysical parameters at the earth's surface. It is required by many models in a variety of fields, including

J. Zhou, Y. Wang, and J. Ma are with the School of Resources and Environment, University of Electronic Science and Technology of China, Chengdu 611731, China (e-mail: jzhou233@uestc.edu.cn; kristenstewert@163.com; jinm92@126.com).

S. Liang is with the State Key Laboratory for Remote Sensing Science and Faculty of Geographical Science, Beijing Normal University, Beijing 100875, China, and also with the Department of Geographical Sciences, University of Maryland, College Park, MD 20742 USA (e-mail: sliang@umd.edu).

J. Cheng is with the State Key Laboratory for Remote Sensing Science and Faculty of Geographical Science, Beijing Normal University, Beijing 100875, China (e-mail: brucechan2003@126.com).

Color versions of one or more of the figures in this paper are available online at http://ieeexplore.ieee.org.

climatology [1], [2], meteorology [3], hydrology [4], and environmental studies [5]. A long-term, high-quality record of LST benefits the analysis of climate trends. Although ground observation provides a straightforward way to measure LST, it is limited over large areas. In contrast, satellite remote sensing, including thermal infrared (TIR) and passive microwave (MW), provides an effective routine to acquire the thermal radiation emitted from the earth's surface, and thus allows for the retrieval of spatially distributed LST. Although MW is more tolerant of clouds [6]–[9], it suffers from coarser spatial resolution, lower accuracy in LST retrieval, and much higher thermal sampling depth than TIR [7]; thus, it cannot satisfy applications at regional or local scales. In the past four decades, numerous algorithms for the estimation of LST under clear-sky conditions by employing satellite TIR remote sensing have been developed by the scientific communities [10]. Typical algorithms include the split-window algorithm (SWA) [11], [12], single-channel algorithm [13], [14], and temperature-emissivity separation (TES) algorithm [15]–[18]. Usage of these algorithms depends on the number and specifications of the TIR channels of the satellite sensor.

A series of satellite LST products with diverse source algorithms, data inputs, spatial and temporal resolutions have been produced since 2000. The most widely utilized product by the scientific communities is the Terra/Aqua MODIS LST/emissivity product family that is released by the National Aeronautics and Space Administration. Onboard the Sun-synchronous polar-orbiting satellites Terra and Aqua, MODIS has 16 middle infrared (MIR) and TIR channels, allowing LST retrieval through different algorithms. They include the 1-km M*D11_L2 swath product and the M*D11A1 tile product from the generalized SWA [12], the M*D11B1 tile product from the day/night algorithm [19], and the M*D21 product from a newly developed TES algorithm for MODIS [16]. Validation shows that the latest MODIS LST products can satisfy the 1.0 K target accuracy in most cases [20]–[22]. As the successor of MODIS, the Visible Infrared Imager Radiometer Suite (VIIRS) onboard the Sumo National Polar-Orbiting Partnership has two MIR and two TIR channels. The currently available VIIRS LST that is released by the National Oceanic and Atmospheric Administration (NOAA) is based on an SWA trained for each of the 17 International Geosphere-Biosphere Programme land cover types [23], [24]; thus, this algorithm implicitly depends on the land surface emissivity (LSE). This product exhibits errors up to 4.0 K over semiarid and arid areas and has a large difference from the MODIS LST product over humid areas [25]. In the near future, a VIIRS LST product will be generated with an LSE-dependent SWA to eliminate surface-type dependence.

The European scientific communities have developed the ATSR LST series. Since 2002, the Advanced Along Track Scanning Radiometer (AATSR) onboard the European Space Agency polar-orbiting satellite, Envisat, has provided a 10-year record of LST with a 1-km resolution. Similar to VIIRS, its source algorithm is an emissivity implicitly dependent SWA, which was trained for each of the 13 biomes and one class representing lakes [26]. The AATSR product was recently improved by a new processor of the University of Leicester based on data inputs with finer resolution [27]. The new product, i.e., GlobTemperature GT_ATS_2P in version 1.0, yields average absolute biases of 1.0 K during daytime and 1.08 K during nighttime [27]. As the successor of AATSR, the Sea and Land Surface Temperature (SLSTR) onboard the Sentinel-3 satellites has good ability in acquiring LST. This product is also generated with the same algorithm as AATSR and its quality is under examination. In addition to the LST products developed and released by the U.S. and Europe, a daily LST product with an approximately 1-km resolution is also available from the Fengyun-3 Visible and Infrared Radiometer (FY3 VIRR), which is operated by the China Meteorological Administration. The VIRR has two TIR channels in 10–12 μm with a nominal resolution of 1.1 km at nadir. The source algorithm of the current VIRR LST product is the generalized SWA, which was adapted according to the spectral response characteristics of the VIRR [28]. Its quality is under examination and validation.

Compared to polar orbiting satellites, geostationary satellites with TIR sensors can provide LST measurements with very high temporal resolution. One frequently used LST product is from the Spinning Enhanced Visible and Infrared Imager (SEVIRI) onboard the Meteosat Second Generation satellite of the European Organization for the Exploitation of Meteorological Satellites (EUMETSAT). The Satellite Application Facility on Land Surface Analysis of EUMETSAT has developed an LST product based on the generalized SWA by employing two TIR channels in 10–12 μm [12], [29]. This product has a 15-min temporal resolution and a 3-km spatial resolution. Validation at three highly homogeneous sites in Africa indicates that the SEVIRI LST can meet the target accuracy of 2.0 K; the bias over these sites is 0.1 K and the root mean square error (RMSE) is 1.6 K [30], [31]. Furthermore, validation over an oak woodland after addressing the problem of viewing and illumination geometries shows that the SEVIRI LST has a bias of 0.26 K and an RMSE of 1.34 K, and it agrees well with the MODIS LST [32]. In addition to the SEVIRI LST product, there are various LST products from other geostationary satellites such as the U.S. Geostationary Operational Environmental Satellites [33], the Chinese Fengyun-2 satellites [34], and the Japanese Himawari satellites [35]. LST products from a geostationary satellite are limited to a fixed region on the earth's surface and, thus, cannot satisfy applications at the global scale. Nevertheless, global LST products are available by merging the retrievals from multiple global-distributed geostationary satellites [36].

The Global Land Surface Satellite (GLASS), the objective of which is to support the climate change and environmental applications on satellite products, has produced 17 global land surface products including 5 in phase I and 12 in phase II. In phase II, global instantaneous LST products for 1983, 1993,

2003, and 2013 were produced. The basic satellite data inputs of GLASS LST are from NOAA-7 AVHRR for 1983, NOAA-14 AVHRR for 1993, and Terra/Aqua MODIS for 2003 and 2013. The target spatial resolutions of the GLASS-AVHRR and GLASS-MODIS LST products are 0.05° and 1 km, respectively. Compared to other satellite LST products, the GLASS LST product has evident characteristics including

1) in order to provide a stable LST retrieval, it was generated through a multialgorithm ensemble approach;
2) considering that satellite LST products before 2000 are extremely rare, historical global LST products in 1983 and 1993 were produced to support the analysis of interdecadal climate change trends; and
3) to avoid biases induced by differences between algorithms, the same algorithm in LST retrieval was applied to both AVHRR and MODIS data.

This paper reviews the development of the GLASS LST algorithm and the product characteristics. A preliminary evaluation of this product is also presented.

II. OVERVIEW OF THE ALGORITHM

Since numerous SWAs have been developed by scientific communities, the GLASS LST product was generated through an ensemble of multiple SWAs instead of developing a new algorithm. Development of the multialgorithm ensemble approach is as follows. First, widely used SWAs were selected as initial candidate algorithms and were trained globally. Second, the candidate SWAs were refined from three respects, including training accuracy, sensitivity to uncertainties of inputs, and testing accuracy. Third, the candidate SWAs with good performance were merged with the Bayesian model averaging (BMA) model and the ensemble approach was used as the source algorithm of the GLASS LST product. Details are presented in the following sections.

A. Training Scheme of Candidate Algorithms

A global atmospheric profile dataset (GAPD) was derived from the widely used SeeBor V5.0 dataset that contains 15 704 global profiles [37] through removing redundant profiles with similar vertical distributions of atmospheric characteristics and relative humidity at any layer higher than 85% [38]. GAPD serves as a basic dataset in training the candidate algorithms listed hereinafter. It has 549 global distributed atmospheric profiles (see Fig. 1), with the surface air temperature (T_a) ranging from 224.25 to 309.05 K and the column water vapor content (w) ranging from 0.014 to 7.939 g·cm^{-2}. Through exploring the T_a–w scatter plot (see Fig. 2), we found that the T_a–w space can be divided into two subspaces at $T_a = 280$ K. When T_a is lower than 280 K, T_a–w has a linear relationship; this subspace represents dry and cold atmospheres existing in high latitude areas, high elevation areas, and some other areas in winter. Such atmospheres are termed cold atmosphere (cold-ATM) hereinafter. When T_a is higher than 280 K, the scatter plot becomes disperse; this subspace represents middle and low latitude areas with different atmospheres, e.g., warm and humid atmospheres and warm but dry atmospheres. Such atmospheres are termed warm atmosphere (warm-ATM) hereinafter. The cold-ATM sub-
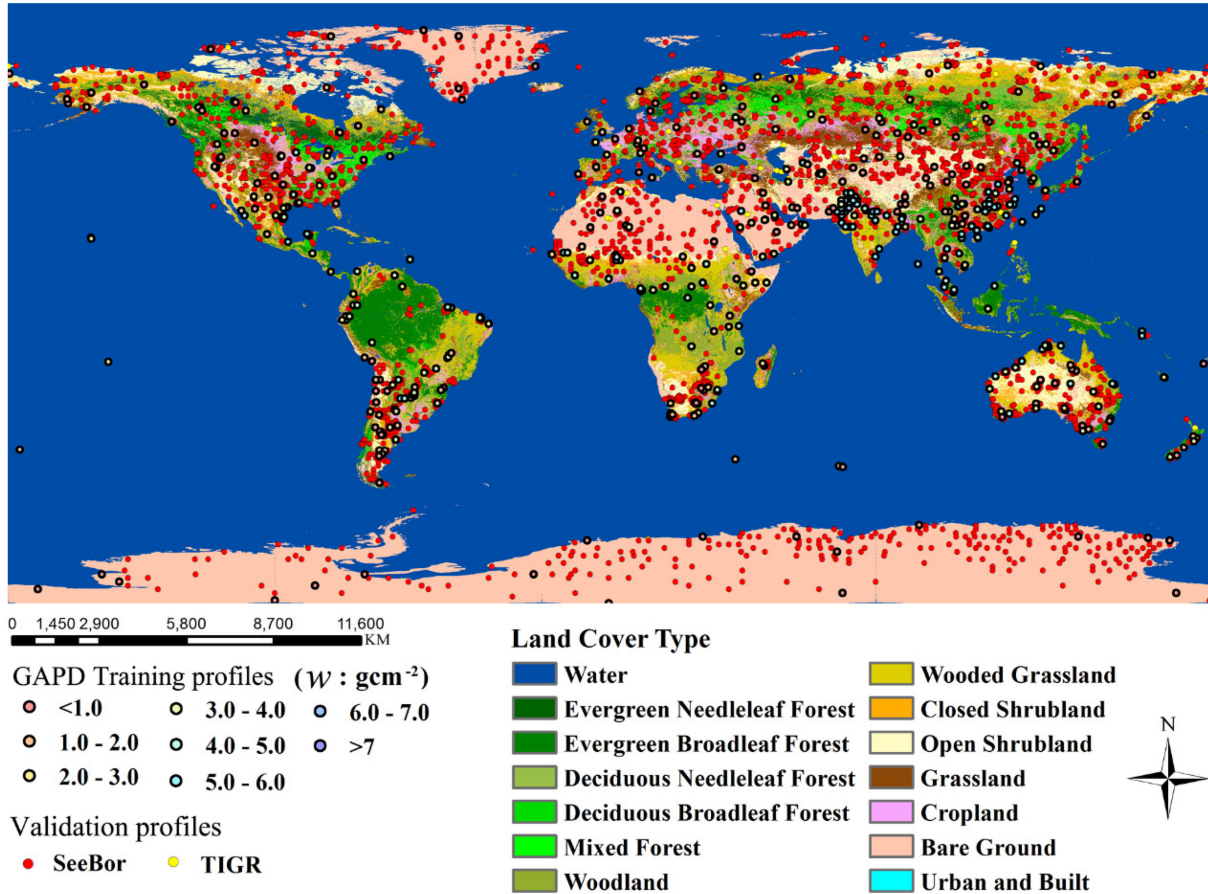
Fig. 1. Spatial distributions of the atmospheric profiles for generating the simulation datasets for training and validating the algorithms. The global land cover type map is from the global AVHRR land cover classification collection [42].
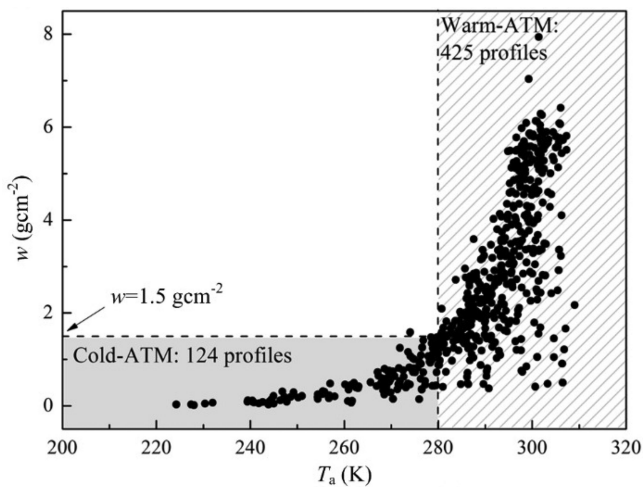

Fig. 2. $T_a - w$ scatter-plot between of the GAPD atmospheric profiles.

set has 124 profiles with w lower than 1.592 g·cm^{-2} and only one profile with w higher than 1.5 g·cm^{-2}; the warm-ATM subset has 425 profiles with w in the range of 0.374–7.928 g·cm^{-2}.

To generate a comprehensive simulation dataset to train the SWAs, 549 profiles were imported into the MODTRAN5 code [39] to implement the forward radiative transfer simulation. For each profile, ten LSTs (from –16 to 20 K with an increment of 4 K) were defined; spectra of 48 materials, includ-ing snow, water, vegetation, and soil, were derived from the Advanced Spaceborne Thermal Emission Reflection Radiometer (ASTER) spectral library [40] and converted to the LSEs in the 11 and 12 μm channels (i.e., ε_{11} and ε_{12}). Ranges of ε_{11} and ε_{12} were 0.674–0.996 and 0.692–0.991 for NOAA-7 AVHRR, 0.670–0.996 and 0.697–0.991 for NOAA-11 AVHRR, and 0.680–0.994 and 0.613–0.991 for MODIS. The view zenith angle (VZA; θ) in the simulation was defined as 0 to 65° with an increment of 5°. MODTRAN5 was executed by utilizing paral-lel cluster computing to speed up the simulation process [41]. After simulation, the training dataset has 3 952 800 samples for each channel, with two at-sensor parameters (i.e., spectral radiance and brightness temperature-T) and three atmospheric parameters (i.e., upwelling radiance, downwelling radiance, and transmittance). According to the noise equivalent delta temper-atures of AVHRR and MODIS, Gaussian-distributed random noises varying from –0.12 to 0.12 K and –0.05 to 0.05 K were added to the simulated brightness temperatures (BT) of AVHRR and MODIS to better simulate the real satellite data.

A regression was conducted based on the training dataset with LST as the dependent variable and ε_{11}, ε_{12}, T_{11}, T_{12}, w, and θ (depending on the SWAs) as the independent variables. Then, the coefficients of each candidate algorithm were deter-mined. The regression was implemented separately for differ-ent atmospheric conditions and θ values. In both cold-ATM and warm-ATM, two intervals of the difference between LST (T_s)

and T_a (i.e., $T_s - T_a$) were chosen, i.e., [−16 K, 4 K] and [−4 K, 20 K], representing nighttime and daytime conditions. Under these two conditions, different subranges of w were defined. For cold-ATM, three subranges of w were defined, including (0, 0.5), (0.5, 1.0), and (1.0, 1.592); the corresponding number of atmospheric profiles was 68, 38, and 18. For warm-ATM, 13 subranges of w were defined, including (0, 0.5), (0.5, 1.0), (1.0, 1.5), (1.5, 2.0), (2.0, 2.5), (2.5, 3.0), (3.0, 3.5), (3.5, 4.0), (4.0, 4.5), (4.5, 5.0), (5.0, 5.5), (5.5, 6.0), and (6.0, 7.928); the corresponding number of the atmospheric profiles was 9, 17, 48, 57, 41, 44, 37, 24, 25, 25, 41, 46, and 11. The regression was implemented for each θ, namely, a total of 14 θ values from 0 to 65° with an increment of 5°. Eventually, there were at least 2592 samples and up to 22 848 in training each candidate algorithm. Therefore, the trained results based on these abundant samples are believable. After the regression, a look-up table of the coefficients under different atmospheric conditions and at different θ values was generated for each candidate algorithm.

B. Initial Selection of Candidate Algorithms

A total of 17 SWAs developed by scientific communities in recent decades are selected as the initial candidate algorithms. Their formulas are listed in Tables I and II. Some of the SWAs have been summarized in [43] and [44]. These SWAs can be divided into two categories according to their inputs: category I requires ε_{11}, ε_{12}, T_{11}, and T_{12} (see Table I) and category II requires additional w (see Table II). Although a path-length term can be added in each SWA [43], it is not considered here because we found it results in limited improvement on SWAs' accuracies [38]. Among the 17 candidate SWAs, the BL1995 of category II is the only SWA that has a cosine term.

In the training process, we found that six (i.e., OV1992, FO1996, FOW1996, UC1985, MT2002, and PP1991) of the 17 SWAs have lower accuracies than the others. By selecting NOAA-7 AVHRR as an example, the standard error of the estimate (SEE) values in the regression for FO1996 is higher than 1.7 K in cold-ATM and 1.4 K in warm-ATM; SEE values for FOW1996 are higher than 2.5 K in cold-ATM and 1.2 K in warm-ATM. Thus, these six SWAs were excluded from the candidate algorithm list.

For each of the other 11 SWAs, the training accuracy for NOAA-7 AVHRR and NOAA-9 AVHRR is similar due to similar channel characteristics; the training accuracy for MODIS shows a slight discrepancy (i.e., 0.15 K in SEE lower) from AVHRR. Due to space limitation, only SEEs of the other 11 candidate SWAs for NOAA-7 AVHRR when $T_s - T_a$ is [−4 K, 20 K] are shown (see Fig. 3). It is evident that most SWAs yield slight discrepancies in training accuracy under a certain atmospheric condition. All 11 SWAs have SEE values lower than 2.2 K. For atmospheric conditions with low w, all of the SWAs have very high training accuracies; the training accuracy decreases when w or θ increases. In cold-ATM with all w subranges and warm-ATM with w less than 2.5 g·cm^{-2} (namely, from W1 to W5), SEE values are generally lower than 0.7 K for AVHRR and 1.0 K for MODIS, indicating very good training accuracy in dry atmospheres. In warm-ATM, SEE increases significantly when w is greater than 4.0 g·cm^{-2}, especially when θ is greater

than 50°. Generally, SWAs of category II have slightly better training accuracies than category I because w is an explicit input in the formulas of category II. Among all the SWAs, SO1991 and CO1994 have the best training accuracy. For example, for NOAA-7 AVHRR, its SEE values are less than 0.37 and 0.39 K in cold-ATM. In contrast, VI1991 has the lowest training accuracy. Similar findings are obtained when $T_s - T_a$ is [−16 K, 4 K].

C. Refined Selection of Candidate Algorithms

To determine stable and accurate SWAs from the remaining 11 candidate SWAs, further assessment including a sensitivity analysis and a global test were performed. The sensitivity analysis was based on the training dataset and LST uncertainties induced by uncertainties of w, ε_{11}, and ε_{12} were quantified. To understand the sensitivities of SWAs under possible atmospheric conditions, a random noise approach was employed in this study. Gaussian-distributed random uncertainties were added to ε_{11}, ε_{12}, and w. Two uncertainty levels were considered, including 1) level 1: maximum $|\delta\varepsilon_{11}| \leq 0.02$, $|\delta\varepsilon_{12}| \leq 0.02$, and $|\delta w| \leq 1.0$ g·cm^{-2}; and 2) level 2: maximum $|\delta\varepsilon_{11}| \leq 0.04$, $|\delta\varepsilon_{12}| \leq 0.04$, and $|\delta w| \leq 1.0$ g·cm^{-2}.

LST uncertainties at each level, expressed by the mean bias error (MBE) and the standard deviation of the error (STD) calculated based on the retrieved LST and the true LST, are shown in Table III. Among the 11 SWAs, SO1991 and CO1994 have the highest sensitivities. Moderate differences between the LST uncertainties at level 1 and level 2 reveal that the two SWAs are slightly sensitive to LSE uncertainty but are very sensitive to CWVC uncertainty. The possible reason for this phenomenon is that there are many terms with w in their formulas. Therefore, SO1991 and CO1994 were excluded from the candidate algorithm list. In contrast, the sensitivity of the other nine SWAs is low, with all LST uncertainties at both level 1 and level 2 lower than 1.60 K. Similar sensitivities were found for AVHRR and MODIS. At level 1, the STD values are lower than 1.21 K (ULW1994) for NOAA-7 AVHRR, 1.11 K (VI1991) for NOAA-11 AVHRR, and 1.20 K (SR2000) for MODIS; BL-WD and WA2014 have the lowest STD values. In fact, the maximum LSE uncertainty of 0.02 may be achieved using practical methods such as the NDVI threshold method [58], whereas the maximum CWVC uncertainty of 1.0 g·cm^{-2} can generally be satisfied by current reanalysis products such as the Modern-Era Retrospective Analysis for Research and Applications (MERRA) [59]. For surfaces with sparse to no vegetation, the uncertainty of LSE may exceed 0.02. At level 2, the LST uncertainties of all SWAs increase approximately 0.2 to 0.4 K, indicating that the SWAs still have acceptable accuracy.

The nine retrained candidate SWAs were further validated based on two global simulation datasets, which were generated through forward atmospheric radiative transfer simulation based on 1) the SeeBor atmospheric profiles over land that were not selected by GAPD and 2) the global thermodynamic initial guess retrieval (TIGR) atmospheric profiles over land (see Fig. 1) [60], [61]. After cloud screening, there are 4761 SeeBor profiles (w: 0.005–4.999 g·cm^{-2}) and 506 TIGR profiles (w: 0.058–8.199 g·cm^{-2}). These two simulation datasets are here-

TABLE I
CANDIDATE SWAs (CATEGORY I) WITH THE COLUMN WATER VAPOR CONTENT (w) AS THE IMPLICIT PARAMETER CONSIDERED FOR THE GLASS LST PRODUCT

No.	SWA	Formula	Source
1	OV1992	$T_s = A_0 + A_1 T_{11} + A_2 (T_{11} - T_{12})$	Ottlé & Vidal-Madjar (1992) [45]
2	FO1996	$T_s = A_0 + A_1 T_{11} + A_2 (T_{11} - T_{12}) + A_3 (T_{11} - T_{12})^2$	François & Ottlé (1996) [46]
3	PR1984	$T_s = A_0 + A_1 T_{11} + A_2 (T_{11} - T_{12}) + A_3 T_{11} \varepsilon_{11} + A_4 (T_{11} - T_{12})(1 - \varepsilon_{11}) + A_5 T_{12} \Delta\varepsilon$	Price (1984) [47]
4	UC1985	$T_s = A_0 + A_1 T_{11} + A_2 (T_{11} - T_{12}) + A_3 (1 - \varepsilon)$	Ulivieri & Cannizzaro (1985) [48]
5	BL-WD	$T_s = A_0 + \left(A_1 + A_2 \dfrac{1-\varepsilon}{\varepsilon} + A_3 \dfrac{\Delta\varepsilon}{\varepsilon^2} \right)(T_{11} + T_{12}) + \left(A_4 + A_5 \dfrac{1-\varepsilon}{\varepsilon} + A_6 \dfrac{\Delta\varepsilon}{\varepsilon^2} \right)(T_{11} - T_{12})$	Becker & Li (1990) [11] and Wan & Dozier (1996) [12]
6	PP1991	$T_s = A_0 + A_1 \dfrac{T_{11} - T_0}{\varepsilon_{11}} + A_2 \dfrac{T_{12} - T_0}{\varepsilon_{12}} + A_3 \dfrac{1 - \varepsilon_{11}}{\varepsilon_{11}} + T_0$	Prata & Platt (1991) [49]
7	VI1991	$T_s = A_0 + A_1 T_{11} + A_2 (T_{11} - T_{12}) + A_3 \dfrac{1-\varepsilon}{\varepsilon} + A_4 \dfrac{\Delta\varepsilon}{\varepsilon}$	Vidal (1991) [50]
8	UL1994	$T_s = A_0 + A_1 T_{11} + A_2 (T_{11} - T_{12}) + A_3 (1 - \varepsilon) + A_4 \Delta\varepsilon$	Ulivieri *et al.* (1994) [51]
9	WA2014	$T_s = A_0 + \left(A_1 + A_2 \dfrac{1-\varepsilon}{\varepsilon} + A_3 \dfrac{\Delta\varepsilon}{\varepsilon^2} \right)(T_{11} + T_{12}) + \left(A_4 + A_5 \dfrac{1-\varepsilon}{\varepsilon} + A_6 \dfrac{\Delta\varepsilon}{\varepsilon^2} \right)(T_{11} - T_{12}) + A_7 (T_{11} - T_{12})^2$	Wan (2014) [21]

Note: 1) $\varepsilon = (\varepsilon_{11} + \varepsilon_{12})/2$, $\Delta\varepsilon = (\varepsilon_{11} - \varepsilon_{12})$; 2) A_i is coefficient; and 3) T_0 in PP1991 is 273.15.

TABLE II
CANDIDATE SWAs (CATEGORY II) WITH THE COLUMN WATER VAPOR CONTENT (w) AS THE EXPLICIT PARAMETER CONSIDERED FOR THE GLASS LST PRODUCT

No.	SWA	Formula	Source
1	FOW1996	$T_s = A_0 + \left(A_1 w + A_2 w^2 + A_3 \right) T_{11} + \left(A_4 w + A_5 w^2 + A_6 \right) T_{12} + A_7 w + A_8 w^2$	François & Ottlé (1996) [46]
2	SO1991	$T_s = A_0 + A_1 T_{11} + \left[A_2 w + A_3 + (A_4 w + A_5)(1 - \varepsilon_{11}) + (A_6 w + A_7) \Delta\varepsilon \right](T_{11} - T_{12})$ $+ \dfrac{1 - \varepsilon_{11}}{\varepsilon_{11}} T_{11} \left[A_8 w + A_9 + (A_{10} w + A_{11}) \Delta\varepsilon \right] - \dfrac{1 - \varepsilon_{12}}{\varepsilon_{12}} T_{12} \left[A_{12} w + A_{13} + (A_{14} w + A_{15}) \Delta\varepsilon \right]$	Sobrino, Coll, & Caselles (1991) [52]
3	ULW1994	$T_s = A_0 + A_1 T_{11} + (A_2 w + A_3)(T_{11} - T_{12}) + (A_4 w + A_5)(1 - \varepsilon) + (A_6 w + A_7) \Delta\varepsilon$	Ulivieri *et al.* (1994) [51]
4	CO1994	$T_s = A_0 + A_1 T_{11} + A_2 (T_{11} - T_{12}) + A_3 (T_{11} - T_{12})^2 +$ $\left[(A_4 w + A_5) T_{11} + (A_6 w + A_7) \right](1 - \varepsilon) - \left[(A_8 w + A_9) T_{11} + (A_{10} w + A_{11}) \right] \Delta\varepsilon$	Coll *et al.* (1994) [53]
5	SR2000	$T_s = A_0 + A_1 T_{11} + A_2 (T_{11} - T_{12}) + A_3 (T_{11} - T_{12})^2 + (A_4 w + A_5)(1 - \varepsilon) - (A_6 w + A_7) \Delta\varepsilon$	Sobrino & Raissouni (2000) [54]
6	MT2002	$T_s = A_0 + A_1 T_{11} + A_2 (T_{11} - T_{12}) + A_3 (T_{11} - T_{12})^2 + (A_4 w + A_5)(1 - \varepsilon)$	Ma & Tsukamoto (2002) [55]
7	BL1995	$T_s = A_0 + A_1 w + \left[A_2 + (A_3 w \cos\theta + A_4)(1 - \varepsilon_{11}) - (A_5 w + A_6) \Delta\varepsilon \right](T_{11} + T_{12})$ $+ \left[A_7 + A_8 w + (A_9 + A_{10} w)(1 - \varepsilon_{11}) - (A_{11} w + A_{12}) \Delta\varepsilon \right](T_{11} - T_{12})$	Becker & Li (1995) [56]
8	GA2008	$T_s = A_0 + A_1 T_{11} + A_2 (T_{11} - T_{12}) + A_3 (T_{11} - T_{12})^2 + \left(A_4 + A_5 w + A_6 w^2 \right)(1 - \varepsilon) + \left(A_7 + A_8 w \right) \Delta\varepsilon$	Galve *et al.* (2008) [57]

Note: Both François and Ottlé and Ulivieri *et al.* proposed two SWAs and one requires w as an input; the corresponding SWAs are abbreviated as "FOW1996" and "ULW1994" in this study.

inafter termed VAL-S and VAL-T, respectively. In the forward simulation, ε_{11} and ε_{12} corresponding to each atmospheric profile were determined according to the land cover type; ten random θ values in the range of 0–65° were defined. Gaussian-distributed random noises were also added to the simulated BT. LSTs were retrieved through the nine candidate SWAs based on ε_{11}, ε_{12}, and w with random uncertainties and were then compared with the predefined LST. MBE and STD of the SWAs were calculated to evaluate their performance, and the results for NOAA-7 AVHRR are shown in Fig. 4.

At level 1, BL-WD, VI1991, and WA2014 yield slight overestimations of LST, with MBE values of 0.15–0.22 K for VAL-S
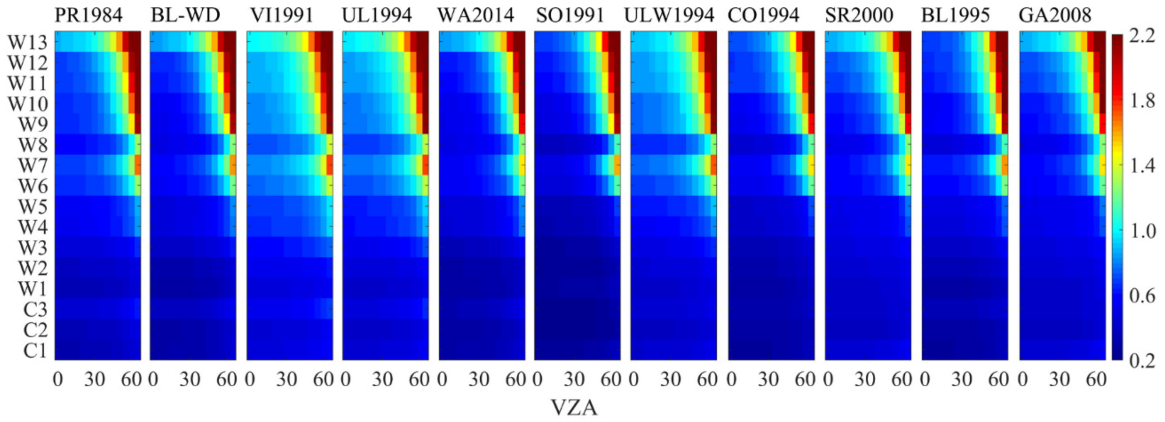
Fig. 3. SEE values of 11 candidate SWAs for NOAA-7 AVHRR under different atmospheric conditions when $T_s - T_a$ is [–4 K, 20 K]. C_i ($i = 1, 2, 3$) and W_j ($j = 1, 2, \ldots, 13$) denote the ith subrange and jth subrange of w in cold-ATM and warm-ATM, respectively.

TABLE III
MBE AND STD VALUES OF 11 CANDIDATE SWAs AT DIFFERENT LEVELS OF LSE AND CWVC
UNCERTAINTIES WHEN EVALUATED BASED ON THE TRAINING DATASET

SWA	NOAA-7 AVHRR				NOAA-11 AVHRR				MODIS			
	Level 1 (K)		Level 2 (K)		Level 1 (K)		Level 2 (K)		Level 1 (K)		Level 2 (K)	
	MBE	STD	MBE	STD	MBE	STD	MBE	STD	MBE	STD	MBE	STD
PR1984	-0.08	1.05	-0.08	1.34	-0.08	1.06	-0.09	1.35	-0.07	1.09	-0.08	1.43
BL-WD	-0.08	1.03	-0.09	1.34	-0.08	1.04	-0.09	1.37	-0.07	1.08	-0.08	1.34
VI1991	-0.07	1.10	-0.08	1.36	-0.07	1.11	-0.08	1.38	-0.07	1.11	-0.08	1.42
UL1994	-0.07	1.07	-0.08	1.32	-0.07	1.07	-0.08	1.34	-0.07	1.09	-0.08	1.41
WA2014	-0.07	1.03	-0.07	1.35	-0.07	1.04	-0.07	1.38	-0.07	1.08	-0.07	1.42
SO1991	4.66	10.05	4.66	10.14	5.06	11.07	5.06	11.16	5.01	9.99	5.02	10.10
ULW1994	-0.07	1.21	-0.07	1.44	-0.07	1.09	-0.08	1.35	-0.07	1.19	-0.08	1.50
CO1994	-1.66	4.44	-1.65	4.52	-1.72	4.43	-1.71	4.52	-1.70	7.08	-1.69	7.17
SR2000	-0.07	1.20	-0.07	1.45	-0.07	1.08	-0.07	1.36	-0.07	1.20	-0.08	1.56
BL1995	-0.09	1.18	-0.09	1.45	-0.09	1.07	-0.09	1.37	-0.09	1.19	-0.10	1.57
GA2008	-0.06	1.04	-0.07	1.32	-0.06	1.05	-0.07	1.34	-0.06	1.09	-0.07	1.46

and 0.07–0.14 K for VAL-T, whereas the other SWAs yield ignorable systematic errors. STD values of all the nine SWAs are lower than 0.82 K with respect to VAL-S and 1.0 K with respect to VAL-T, demonstrating good accuracy under possible atmospheric conditions at the global scale. Among the nine SWAs, BL-WD and WA2014 have the lowest STD values, although the differences between their STD values and the other seven SWAs are small.

At level 2, both the MBE and STD values of every SWA increase as expected. However, the increases in errors are different because the SWAs have different sensitivities. All nine SWAs yield overestimations on LST when they are evaluated based on VAL-S and VAL-T. For VAL-S, UL1994 has the lowest MBE

(0.18 ± 1.25 K), whereas VI1991 has the highest MBE (0.39 ± 1.23 K); for VAL-T, ULW has the lowest MBE (0.11 ± 1.46 K), and VI1991 has the highest MBE (0.36 ± 1.44 K). Furthermore, the optimal algorithms are different under different atmospheric conditions, for different uncertainties of inputs, and different land cover types (representing by LSE values). Very similar findings were obtained for NOAA-11 AVHRR and MODIS.

D. Multialgorithm Ensemble Approach

Since none of the candidate algorithms can obtain the best performance under every condition, a multialgorithm ensemble approach is expected to yield a more stable LST estimate than
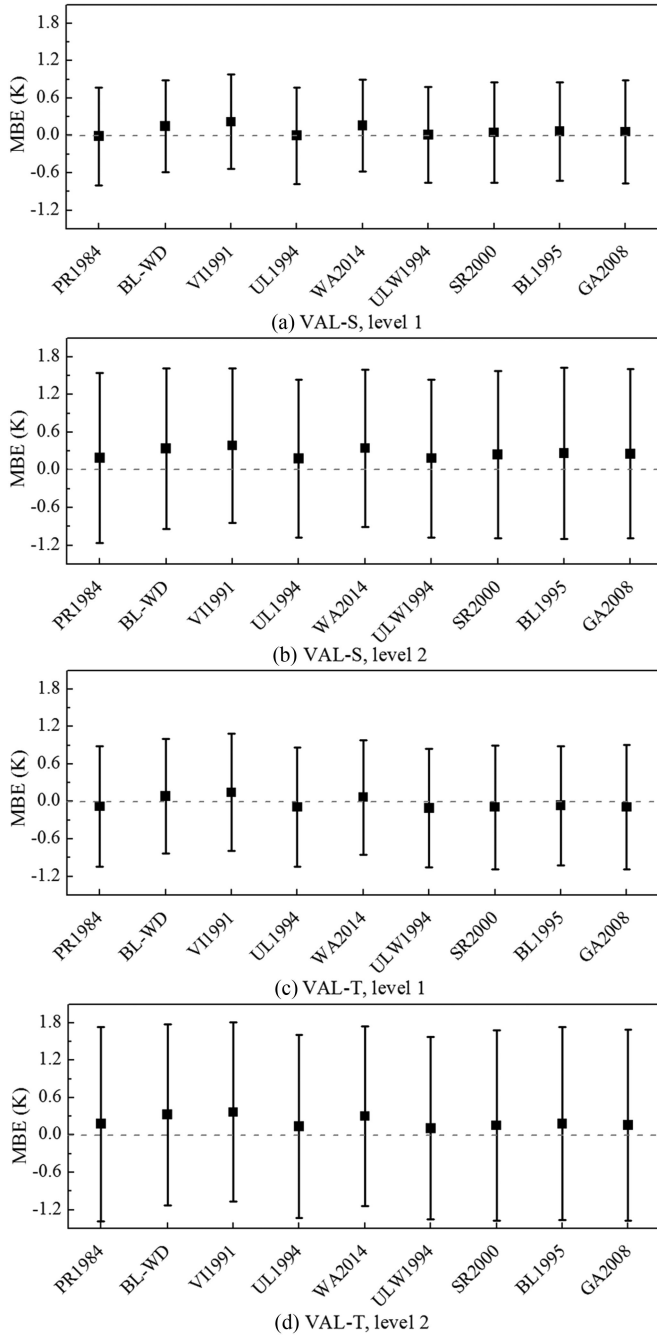
Fig. 4. MBE and STD values of nine SWAs for NOAA-7 AVHRR data based on VAL-S and VAL-T.

a single algorithm. The BMA model is employed here to combine the estimates of different candidate SWAs. Recently, BMA has exhibited good performance in the combinations of multiple models for surface longwave radiation and surface evapotranspiration [62], [63].

Assuming that 1) there are K SWAs $\{f_1, f_2, \ldots, f_K\}$ and 2) the LST estimate from a candidate SWA is r and the corresponding true value of LST is r_t, the probability density function (PDF) of r based on the multialgorithm ensemble is [62], [64]

$$p\left(r|\,f_1, f_2, \ldots, f_K\right) = \sum_{k=1}^{K} p\left(r|\,f_k\right) p\left(f_k|\,r_t\right) \qquad (1)$$

where $p(r|f_k)$ is the predictive PDF based on f_k and $p(f_k|r_t)$ is the posterior probability of f_k.

The sum of the posterior probabilities of all SWAs is 1, and they can be treated as the weights of the corresponding algorithms in the combination of multiple algorithms. Thus, (1) can be converted to

$$p\left(r|\,f_1, f_2, \ldots, f_K\right) = \sum_{k=1}^{K} \omega_k p\left(r|\,f_k\right) \qquad (2)$$

where w_k is the weight of SWA f_k.

It is reasonable to assume that $p(r|f_k)$ has a Gaussian distribution with a mean value $\overline{f_k}$ and a variance σ_k^2 [62]–[64]. Assuming the parameter vector $\theta_k = \{\overline{f_k}, \sigma_k^2\}$ and a conditional density function $g(\cdot)$, we have

$$p\left(r|\,f_k\right) = g\left(r|\,\theta_k\right) \qquad (3)$$

$$p\left(r|\,f_1, f_2, \ldots, f_K\right) = \sum_{k=1}^{K} \omega_k g\left(r|\,\theta_k\right). \qquad (4)$$

Then, the LST estimate based on the multialgorithm ensemble is the conditional expectation of r:

$$E\left[r|\,f_1, f_2, \ldots, f_K\right] = \sum_{k=1}^{K} w_k \overline{f_k}. \qquad (5)$$

The key step for BMA is the determination of the weight of each individual SWA (i.e., ω_k). We followed the maximum likelihood method [62], [64]. Since it is impossible to obtain abundant *in situ* measured LSTs at the global scale in the determination of ω_k, we used the aforementioned training dataset. A total of nine candidate SWAs (i.e., R1984, BL-WD, VI1991, UL1994, WA2014, ULW1994, SR2000, BL1995, and GA2008) were combined in BMA. The BMA models were trained under 32 atmospheric conditions.

The weights of the nine SWAs in the BMA model were calculated at the aforementioned two uncertainty levels. For barren land, the LSE of which may have great uncertainty, the weights at level 2 were used; for the other land cover types, the weights at level 1 were used. The weights of the nine SWAs under three atmospheric conditions in cold-ATM and warm-ATM for NOAA-7 AVHRR data are shown in Fig. 5. All SWAs in the BMA model have weights in the range from 0.10 to 0.13, indicating that they have similar contributions to the LST estimate. Nevertheless, their weights have slight differences. For example, when w is less than 0.5 g·cm^{-2} in cold-ATM at level 1, UL1994, ULW1994, and BL1995 have higher weights (0.115–0.120) than the other seven SWAs because the former three SWAs have better accuracies; when w increases, their weights decrease and the weights of the other SWAs increase. When w is 5.0–6.0 g·cm^{-2}, BL1995 has the highest weight (0.129) among the nine SWAs; but under the other atmospheric conditions that are shown in Fig. 5, the nine SWAs have very similar weights. The highest weight of BL1995 indicates the best accuracy of BL1995 when w is 5.0–6.0 g·cm^{-2}. The possible reason for this phenomenon is that the cosine term of BL1995 (see Table II) can account for the atmospheric water vapor effects due to variable path-length. When the uncertainty of LSE increases from 0.02
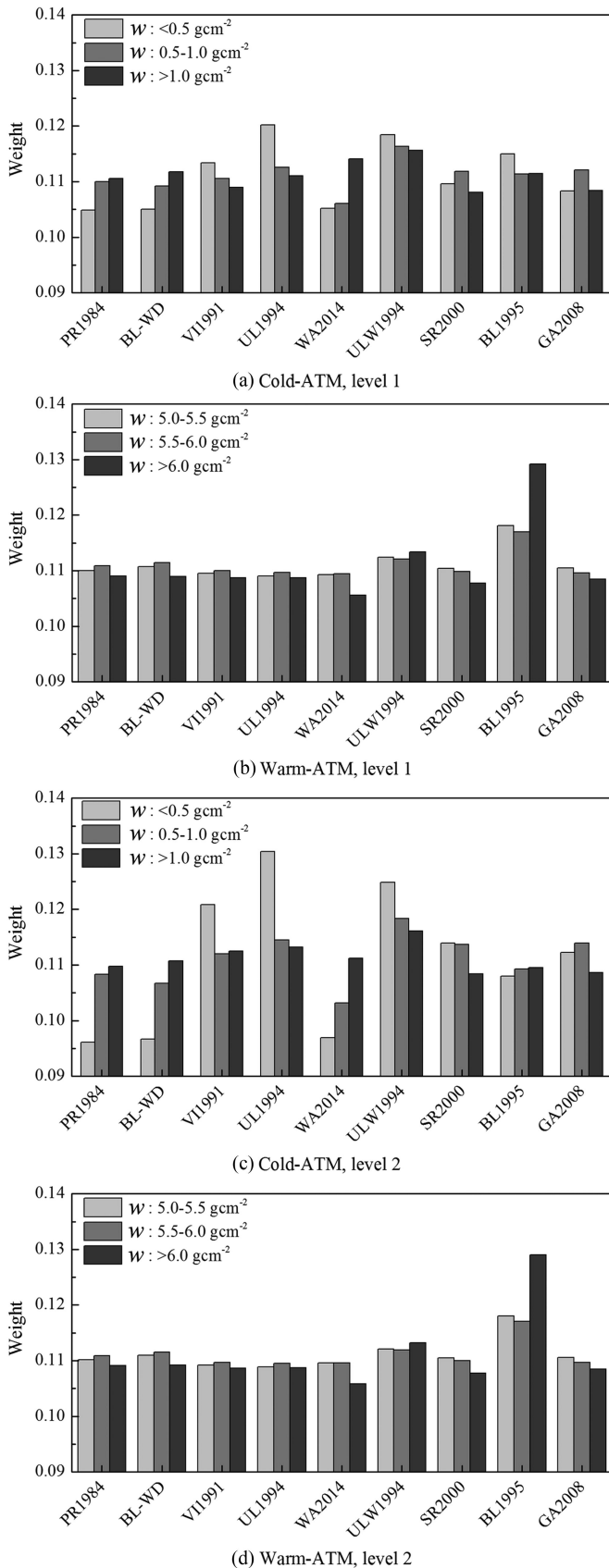
Fig. 5. Weights of different SWAs in the BMA models for NOAA-7 AVHRR data under six atmospheric conditions.

(i.e., level 1) to 0.04 (i.e., level 2), differences between weights of SWAs increase in cold-ATM because the SWAs have many different performances. However, in warm-ATM, the weights of the SWAs at level 2 are similar to those at level 1.

III. PRODUCT CHARACTERISTICS AND APPLICATIONS

A. Product Generation Executive Scheme

Land cover type, vegetation index, and soil type, which were used to determine ε_{11} and ε_{12}, are three basic inputs of the product generation executive (PGE) code of the GLASS LST product. In the generation of GLASS-AVHRR LST, the global AVHRR land cover classification data released by the Global Land Cover Facility of the University of Maryland and the global daily AVHRR NDVI product (AVH13C1) released by the Land Long Term Data Record (LTDR) of Goddard Space Flight Center were used. For GLASS-MODIS LST, the global MODIS land cover product (i.e., MCD12Q1) and the global 16-day MODIS vegetation index (i.e., M*D13A2) were used. The global soil regions map released by the United States Department of Agriculture was employed to identify the soil type of each AVHRR/MODIS pixel to better determine the LSEs because the LSE of soil shows significant variation [65].

The estimation of ε_{11} and ε_{12} followed a hybrid approach instead of being simultaneously estimated with LST through a TES algorithm. The main reason was that the TES algorithm has limitations for AVHRR data. The hybrid approach included the following stages. First, water, snow/ice, urban, and bare soil pixels were identified; their LSEs were determined based on the convolution of the corresponding spectra derived from the ASTER spectral library with the spectral response functions of the target channel [38], [65]. Second, the NDVI threshold method was applied to the partially vegetated and fully vegetated pixels [66]. Note that the soil type and vegetation type have been taken into account in the determination of LSEs.

In addition to ε_{11} and ε_{12}, w and T_a are two other input datasets of the PGE code. They were derived from the MERRA product, which provides global hourly meteorological parameters at a resolution of $1/2° \times 2/3°$ (namely, 361×540 grids). For a target AVHRR/MODIS pixel, the nearest neighbor method was utilized to extract w and T_a from the MERRA data.

The PGE code was composed based on five modules and was executed on a high-performance computing platform. Module I read the input datasets, including the BTs of the TIR channels (namely, LTDR AVH02C1 for AVHRR and M*D021KM for MODIS), the LUTs of the SWA's coefficients and BMA weights, and the aforementioned datasets. Module II determined w and T_a, and module III determined ε_{11} and ε_{12} of each pixel. Module IV estimated LSTs with the nine SWAs and merged the LST estimates with the BMA model. Module V output the eventual LST and associated scientific datasets, including LST quality control, view time, VZA, latitude, and longitude.

In the PGE code, there were four specific steps. First, for AVHRR, the determination of ε_{11} and ε_{12} for both daytime and nighttime data was based on the monthly composited AVH13C1 product. Second, an interpolation procedure was applied to
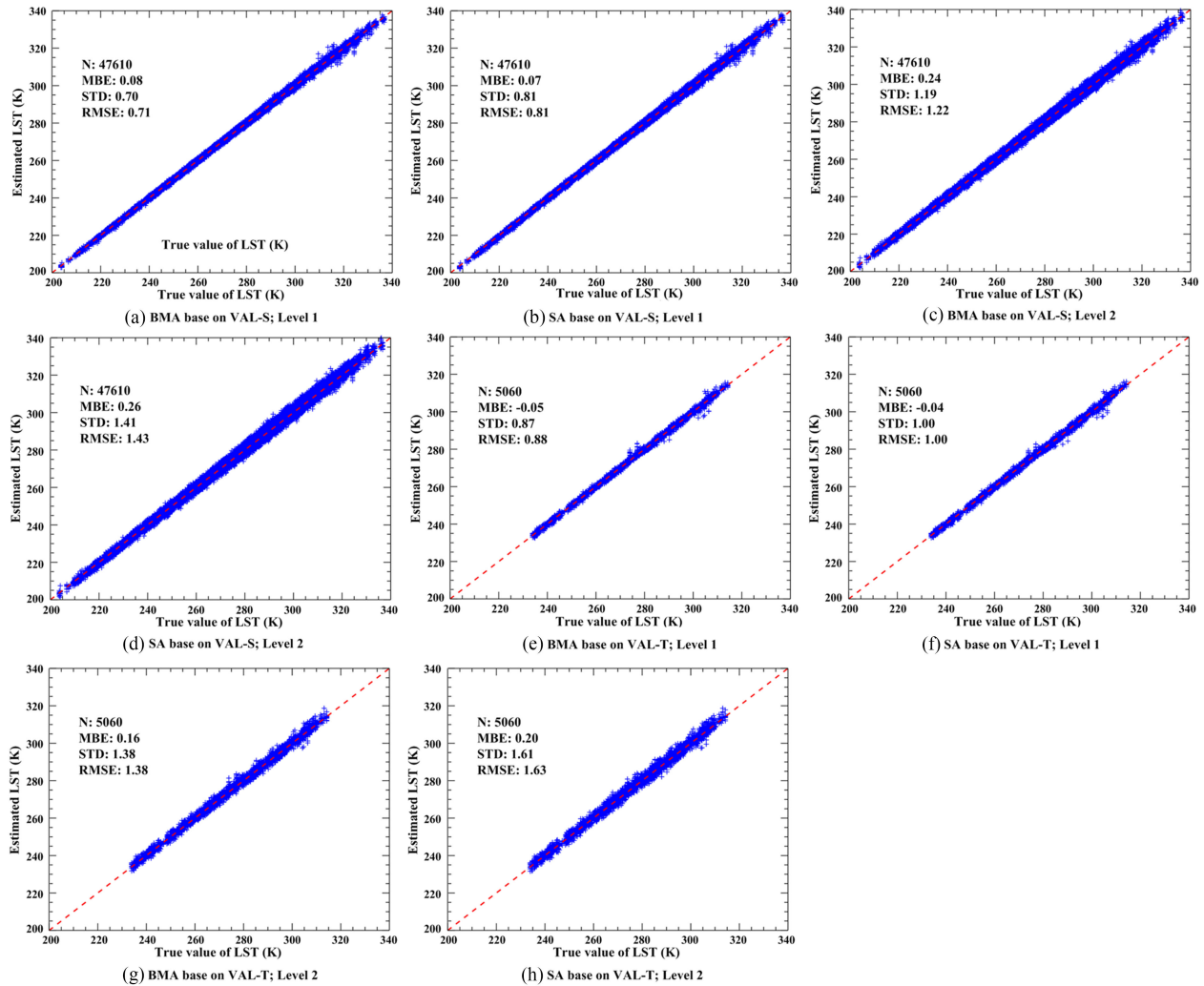
Fig. 6. Validation of the BMA and SA models for MODIS data based on VAL-S and VAL-T (unit of LST is K).

precisely determine the coefficients from the LUTs for each pixel according to its VZA. Third, the coefficients and BMA weights trained at level 2 were used for bare soil pixels to address the possible large uncertainties of their LSEs. Finally, an iteration procedure was employed to determine an accurate $T_s - T_a$ range.

B. Validation Based on Simulation Datasets

The dataset generated through the forward atmospheric radiative transfer simulation allows an "ideal" validation of LST algorithms because the simulation dataset has ignorable noise, and thus can reflect the performance of the algorithm by avoiding noises or uncertainties that are involved with the validation based on *in situ* LST. Thus, the BMA model for generating the GLASS LST product was first validated based on the aforementioned VAL-S and VAL-T. For comparison purposes, the LST retrieved through simple averaging (SA) of the estimate of the SWAs was also validated.

We found that the LST estimated with the BMA model generally yields better accuracy than the individual SWAs. The results for the MODIS data are shown in Fig. 6. At level 1, the BMA model shows ignorable systematic error (MBE = 0.08 K

for VAL-S and MBE = –0.05 for VAL-T). Since the individual SWAs yield diverse systematic errors (see Fig. 4), it is obvious that the ensemble estimation avoids evident overestimation or underestimation. In contrast, slight overestimation of the BMA model can be found at level 2 because all individual SWAs yield slight overestimation at level 2. As expected, the error of the ensemble estimation of LST increases when the LSE uncertainty increases because the accuracies of the individual SWAs decrease.

Generally, the BMA model has better accuracy than the candidate SWAs. For example, its RMSE is 0.88 K at level 1 for VAL-T, whereas the RMSEs of the nine SWAs range from 0.93 K (BL-WD) to 1.09 K (GA2008); at level 2, the RMSE of the BMA model is 1.38 K, which is also lower than the SWAs (from 1.40 K for BL-WD to 1.82 K for BL1995). The BMA model also has better accuracy than the SA model. As shown by Fig. 6, the RMSE of the BMA model is 0.10 K/0.12 K (level 1) or 0.21 K/0.25 K (level 2) lower than the SA model for VAL-S/VAL-T. Since the dataset for training the BMA model is independent from the validation datasets, this finding demonstrates that the multialgorithm ensemble approach can determine more accurate weights of the individual SWAs depending on their performance. Good accuracy of the BMA model also suggests

TABLE IV
VALIDATION OF THE GLASS-AVHRR LST PRODUCT IN 1993
BASED ON *In Situ* LST AT THE BARROW SITE

DOY	GLASS-AVHRR LST (K)	*In situ* LST (K)	Bias error (K)
186	284.30	285.99	-1.69
193	298.55	296.36	2.19
194	293.24	299.32	-6.08
196	292.62	291.35	1.27
199	282.72	284.72	-2.0
204	290.05	290.52	-0.47
205	290.88	289.36	1.52
206	283.07	281.98	1.09
209	289.52	290.59	-1.07
230	286.3	284.93	1.37
231	286.79	284.61	2.18
259	277.62	280.35	-2.73
295	258.59	264.92	-6.33
Overall	RMSE=2.89 K		

that the source algorithm of the GLASS LST product has good applicability.

C. Validation Based on Ground Measurements

The GLASS LST product is currently in the preliminary validation stage, in which the LST product is validated against the ground measured LST and is compared to other satellite LST products. Since *in situ* LSTs were rare in 1983, we obtained the longwave radiation measurements for 1993 at the Barrow site (latitude: 71.32 °N; Longitude: 156.61 °W; elevation: 11 m a.s.l.) of the Baseline Surface Radiation Network (BSRN), at which the interval for longwave radiation observation was 3 min. The longwave radiation was converted to the ground LST according to Stefan–Boltzmann's law [67]. After removing abnormal ground measurements and pixels obscured by cloud contamination, we only obtained 13 pairs of GLASS-AVHRR LST and *in situ* LST in the summer and autumn of 1993. Results are shown in Table IV. A slight underestimation of LST was found, with an MBE of –0.83 K and an RMSE of 2.89 K, revealing that the GLASS LST may satisfy the target accuracy of 3.0 K for NOAA AVHRR. Note that two pairs in Table IV show significant underestimation of LST by the GLASS-AVHRR product; the possible reason is subpixel cloud contamination. Nevertheless, it should be noted that such limited match-ups cannot provide sufficiently reliable validation results; more in-depth examinations of the quality of the GLASS-AVHRR LST product are still needed. Additionally, an alternative means

to evaluate the GLASS-AVHRR LST is to use the historical T_a data, especially over densely vegetated surfaces.

For the validation of the GLASS-MODIS LST product, the widely used ground measurements of longwave radiation of the surface radiation network (SURFRAD) operated by NOAA were collected. Seven sites, including Boulder, CO (sparse grassland), Bondville, IL (grassland), Goodwin Creek, MS (grassland), Fort Peck, MT (grassland), Desert Rock, NV (arid shrubland), Penn State University, PA (cropland), and Sioux Falls, SD (grassland), were selected. The NDVI derived from the M*D13A2 product was first examined to understand the possible intra-annual variation of landscape surrounding these sites. We found that the Desert Rock site has a very stable landscape in an annual cycle (mean value/STD of NDVI in 2003: 0.14/0.02). In contrast, the other five sites have evident variations. For example, the mean value/STD of NDVI for the Fort Peck site was 0.25/0.20 in 2003. Thus, in order to mitigate the scale mismatch between a site and the corresponding pixel and avoid the possible uncertainty induced by surface emissivity that is needed in the conversion of measured surface longwave radiation to LST, only the longwave radiation measurements in the vegetation growth stage (from May to September) were used at all of the sites except Desert Rock. Nevertheless, one should keep in mind that these sites have different spatial representativeness [25], [68]; furthermore, the broadband surface emissivity required in the derivation of *in situ* LST is not easy to determine. In this study, a constant value of broadband surface emissivity was defined for every site according to [25].

The results for the validation of the GLASS-MODIS LST product in 2003 and 2013 are shown in Table V. For comparison purposes, the results of the official MODIS LST product (i.e., M*D11_L2) are also shown. For the seven sites, the RMSE ranges of the daytime GLASS-MODIS LST are 2.87–4.43 K (2003)/2.95–4.27 K (2013) for Terra MODIS and 2.60–4.83 K (2003)/2.72–3.89 K (2013) for Aqua MODIS; the corresponding MBE ranges are –3.07 to 1.21 K (2003)/–2.54 to 1.41 K (2013) for Terra MODIS and –2.54 to 1.41 K (2003)/–2.42 to 0.72 K (2013) for Aqua MODIS. In contrast, the nighttime RMSE ranges are 1.30–5.38 K (2003)/1.51–5.47 K (2013) for Terra MODIS and 1.65–6.01 K (2003)/1.43–6.02 K (2013) for Aqua MODIS. The corresponding MBE ranges are –4.31 to 1.89 K (2003)/–4.66 to 1.99 K (2013) for Terra MODIS and – 4.84 to 1.09 K (2003)/–5.23 to 1.86 K (2013) for Aqua MODIS. A closer examination of Table V indicates that the GLASS-MODIS LST has much better accuracy at nighttime than during the daytime at all site except Desert Rock because the scale mismatch between the site and the pixel decreases at nighttime due to a weaker spatial heterogeneity of LST [8], [31]. For the six grassland/cropland sites, the mean MBE/RMSE values for 2003 are –0.03 K (STD: 1.43)/1.82 K (STD: 0.49 K) for Terra MODIS and –0.19 K (STD: 0.81 K)/1.92 K (STD: 0.19 K) for Aqua MODIS; the mean MBE/RMSE values for 2013 are similar: 0.19 K (STD: 1.31 K)/2.15 K (STD: 0.35 K) for Terra MODIS and 0.38 K (STD: 1.21 K)/1.91 K (STD: 0.45 K) for Aqua MODIS.

TABLE V
VALIDATION OF THE GLASS-MODIS LST PRODUCT BASED ON *In Situ* LST AT SURFRAD SITES (UNIT IS K)

Year	Site	Daytime LST (MBE / RMSE)				Nighttime LST (MBE / RMSE)			
		GLASS (Terra)	M*D11_L2 (Terra)	GLASS (Aqua)	M*D11_L2 (Aqua)	GLASS (Terra)	M*D11_L2 (Terra)	GLASS (Aqua)	M*D11_L2 (Aqua)
	Fort Peck, MT	-0.65 / 3.71 (47)	-1.28 / 3.70 (47)	-0.96 / 2.80 (65)	-1.51 / 2.85 (65)	-1.39 / 2.01 (53)	-2.72 / 3.07 (53)	-0.51 / 2.07 (76)	-1.50 / 2.40 (76)
	Desert Rock, NV	-1.04 / 4.18 (208)	-1.74 / 3.22 (208)	-1.39 / 4.83 (208)	-2.26 / 4.22 (208)	-4.31 / 5.38 (215)	-3.68 / 4.22 (215)	-4.84 / 6.01 (225)	-3.85 / 4.08 (225)
	Bondville, IL	-0.09 / 3.18 (49)	-1.42 / 3.50 (49)	1.25 / 4.50 (69)	0.18 / 4.27 (69)	0.49 / 1.38 (50)	-0.87 / 1.49 (50)	-0.43 / 2.17 (95)	-0.63 / 1.72 (95)
2003	Goodwin Creek, MS	-3.07 / 4.11 (32)	-4.13 / 4.96 (32)	-2.05 / 4.11 (41)	-3.32 / 3.83 (41)	1.89 / 2.28 (27)	0.53 / 1.53 (27)	0.01 / 1.94 (82)	0.14 / 1.94 (82)
	Boulder, CO	1.21 / 4.43 (69)	0.18 / 4.27 (69)	1.17 / 4.60 (82)	-0.41 / 4.63 (82)	-1.82 /2.44 (71)	-2.21 / 2.66 (71)	-1.36 / 1.91 (94)	-1.88 / 2.25 (94)
	Sioux Falls, SD	-3.07 / 4.07 (55)	-4.25 / 4.91 (55)	-1.53 / 2.77 (42)	-2.91 / 3.88 (42)	-0.39 / 1.30 (63)	-1.52 / 1.89 (63)	0.04 / 1.65 (70)	-1.09 / 1.53 (70)
	Penn State U., PA	-1.35 / 2.87 (23)	-2.19 / 3.55 (23)	-0.56 / 2.60 (80)	-1.57 / 2.82 (80)	1.03 / 1.48 (25)	0.01 / 1.19 (25)	1.09 / 1.75 (39)	0.21 / 1.71 (39)
	Fort Peck, MT	1.41 / 3.35 (101)	0.71 / 2.89 (101)	0.72 / 3.33 (52)	0.26 / 2.70 (52)	-0.59 / 2.15 (95)	-1.52 / 2.39 (95)	0.60 / 1.45 (55)	-0.28 / 1.08 (55)
	Desert Rock, NV	-1.96 / 4.27 (277)	-2.30 / 3.52 (277)	-1.81 / 3.88 (218)	-2.15 / 3.02 (218)	-4.66 / 5.47 (282)	-3.42 / 3.68 (282)	-5.23 / 6.02 (236)	-3.93 / 4.22 (236)
	Bondville, IL	-1.14 / 2.95 (58)	-2.47 / 3.81 (58)	-1.30 / 3.81 (35)	-2.73 / 4.33 (35)	-0.12 / 1.51 (81)	-0.97 / 1.76 (81)	0.06 / 1.43 (42)	-0.72 / 1.54 (42)
2013	Goodwin Creek, MS	-2.54 / 3.77 (73)	-3.63 / 4.57 (73)	-2.42 / 3.89 (38)	-3.66 / 4.80 (38)	1.99 / 2.57 (86)	0.79 / 1.81 (86)	1.86 / 2.46 (27)	0.90 / 1.90 (27)
	Boulder, CO	-0.60 / 2.96 (63)	-1.85 / 3.49 (63)	-0.94 / 3.72 (40)	-2.19 / 4.41 (40)	-1.72 / 2.35 (86)	-2.16 / 2.61 (86)	-1.77 / 2.36 (47)	-2.15 / 2.67 (47)
	Sioux Falls, SD	-1.63 / 3.48 (81)	-2.60 / 3.95 (81)	-1.51 / 3.01 (55)	-2.29 / 3.33 (55)	0.37 / 2.18 (87)	-0.42 / 2.20 (87)	0.59 / 1.72 (46)	-0.24 / 1.63 (46)
	Penn State U., PA	-1.52 / 3.77 (36)	-1.94 / 3.81 (36)	-0.18 / 2.72 (34)	-0.95 / 2.65 (34)	1.18 / 2.14 (42)	0.63 / 1.73 (42)	0.95 / 2.02 (35)	0.45 / 1.92 (35)

Note: Numbers in brackets are the numbers of the match-ups.

For the official M*D11_L2 product, we also found that large errors exist for daytime cases. Using 2003 as the example, the daytime RMSE ranges are 3.22–4.96 K for Terra MODIS and 2.82–4.63 K for Aqua MODIS; the corresponding MBE ranges are –4.13 to 0.18 K and –3.32 to 0.18 K. Similar magnitudes of daytime error for the official MODIS LST product have been reported in [68] and have also been reported for the VIIRS LST product [25]. Much better accuracy can be found for nighttime cases. The nighttime RMSE ranges are 1.19–4.22 K for Terra MODIS and 1.53–4.08 K for Aqua MODIS; the corresponding MBE ranges are –3.68 to 0.53 K and –3.85 to 0.21 K. For all sites except Desert Rock, the mean MBE/RMSE values for 2003 are –1.13 K (STD: 1.26 K)/1.97 K (STD: 0.74 K) for Terra MODIS and –0.79 K (STD: 0.88 K)/1.93 K (STD: 0.34 K) for Aqua MODIS; the mean MBE/RMSE values for 2013 are –0.61 K (STD: 1.17 K)/2.08 K (STD: 0.37 K) for Terra MODIS and –0.34 K (STD: 1.06 K)/1.79 K (STD: 0.53 K) for Aqua MODIS. A comparison between the nighttime GLASS-MODIS and M*D11_L2 products demonstrates that the differences in their accuracies are not significant: the former product has slightly better accuracy for 2003 cases, but slightly lower accuracy for 2013 cases. A comparison of the MBE values shows that the GLASS-MODIS LST yields lower biases than the M*D11_L2 LST. This finding suggests that the multialgorithm ensemble approach of the GLASS LST product can avoid the systematic bias that is involved in a single algorithm.

Table V shows that significant underestimation occurs for both GLASS-MODIS and M*D11_L2 products at the Desert Rock site. We believe that such underestimation mainly arises from the uncertainties of ε_{11} and ε_{12} associated with the arid shrubland, which are very difficult to determine due to large variations in surface spectral emissivity [25], [68]. Furthermore, GLASS-MODIS LST has lower accuracy at nighttime than during the daytime at this site. This finding is opposite to the findings from the other six grassland/cropland sites and the M*D11_L2 product. Considering that the MERRA product may have larger uncertainties over deserts [69], a possible reason may be the uncertainty associated with T_a that is input into the PGE code of GLASS-MODIS LST product. These results indicate that the GLASS LST product needs further improvements in regions with arid shrublands and deserts.

D. Demonstration of GLASS LST Product

Figs. 7 and 8 present two granule-based MODIS LST maps, as well as LSEs and NDVI at 1-km resolution. These two granules are from over the southern and western United States, respectively. The two figures show that the spatial patterns of the LSEs are closely related to the NDVI: regions with higher vegetation cover have higher LSEs, and vice versa. The MODIS LST maps exhibit reasonable LST patterns. Fig. 7 indicates that regions with higher vegetation cover are much warmer than the regions with lower vegetation cover, because vegetation has good insulation capacity at nighttime. In contrast, the barren land with very low vegetation cover is much warmer than the vegetated surfaces due to low thermal inertia and evaporation during daytime and in summer, as shown in Fig. 8.

The two GLASS-MODIS LST maps were further compared with the official MODIS LST maps of collection 6 (MOD11_L2 on DOY 1 and MYD11_L2 on DOY 181). The results of the comparison are shown in Fig. 9. The mean bias deviation (MBD)/root mean square deviation (RMSD) is –1.19 K/1.87 K

(a) LST   (b) NDVI

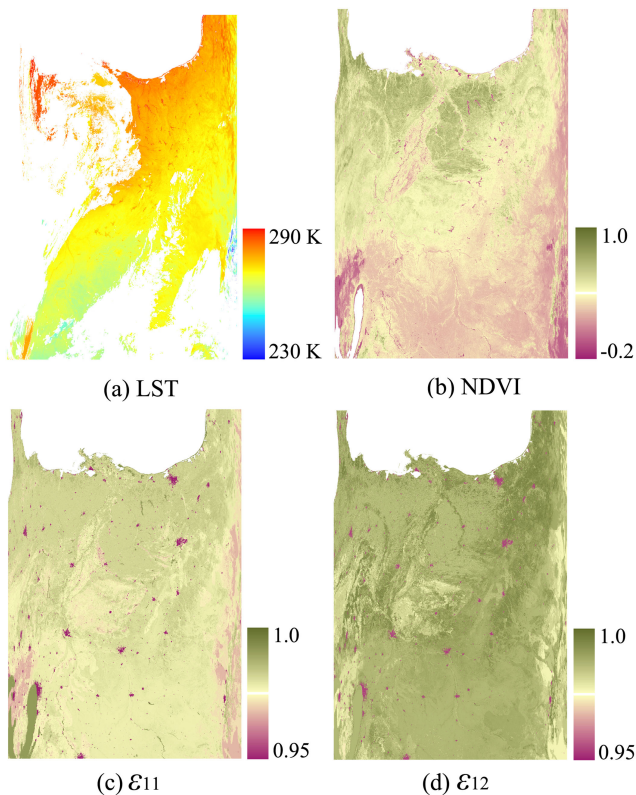(c) ε_{11} (d) ε_{12}

Fig. 7.   GLASS-MODIS LST map over the southern U.S. at 04:20 (UTC, hereinafter the same) on DOY 1 in 2003. The pixels in white color are masked due to clouds and sea/ocean. NDVI, ε_{11}, and ε_{12} are also shown. Note that the upward direction of the maps is south and the downward direction is north.
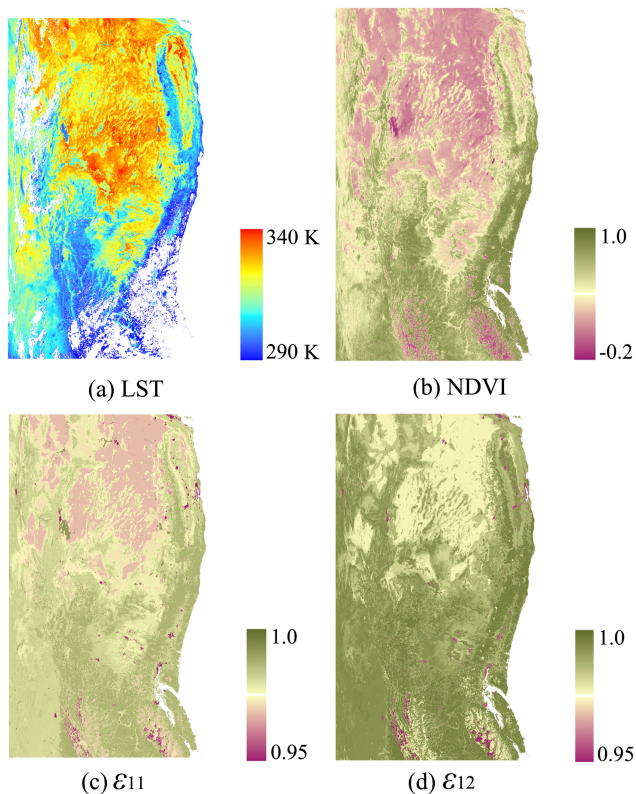

(a) LST   (b) NDVI

(c) ε_{11} (d) ε_{12}

Fig. 8.   Same as Fig. 7 but for the western U.S. on DOY 181 in 2003.
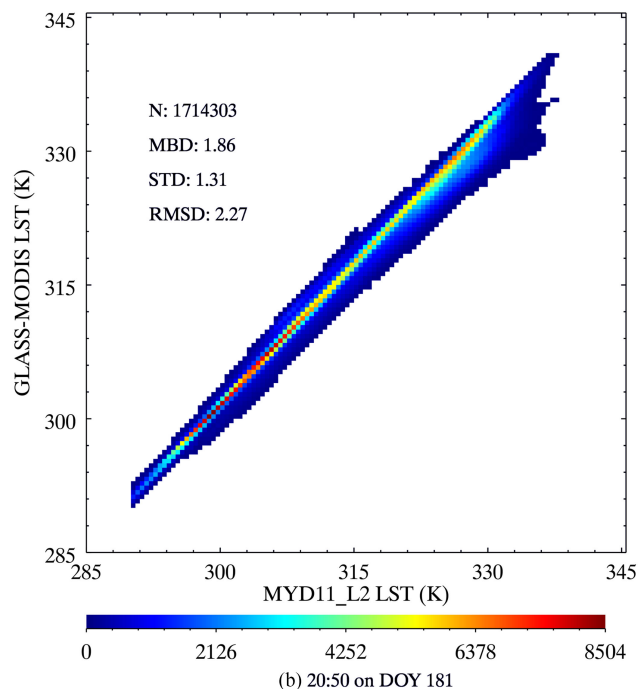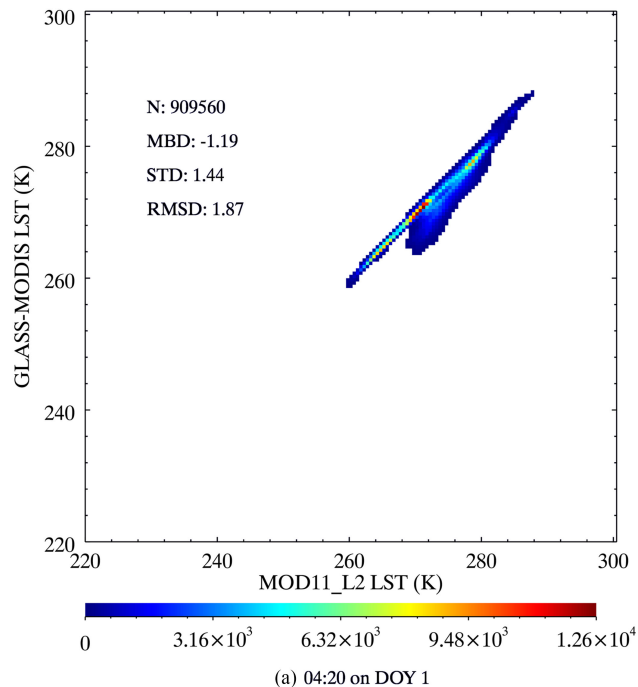

(a) 04:20 on DOY 1

(b) 20:50 on DOY 181

Fig. 9.   Density plots between the GLASS LST and the official MODIS LST (M*D11_L2).

and 1.89 K/2.27 K, indicating that these two independent LST products agree well with each other. Although significant positive (negative) deviation was found for the swath on DOY 1 (DOY 181), comparison between these two granules suggests no systematic deviation exists between the two LST products. The deviation may be contributed by the differences between the source algorithms and the input datasets. According to the global training and validation of the algorithm of the GLASS

LST product, it is evident that the algorithm is reliable. Thus, a further comparison was conducted between the input ε_{11}, ε_{12}, and w of the GLASS LST and M*D11_L2 LST. Some interesting findings were obtained. For the first swath, a negative deviation was found for ε_{11} (–0.004 $\pm$ 0.005) and a positive deviation was found for ε_{12} (0.001 $\pm$ 0.005); for the second swath, the deviations for ε_{11} and ε_{12} are 0.004 $\pm$ 0.006 and –0.001 $\pm$ 0.006, respectively. The corresponding deviations for w are 1.435 $\pm$ 0.646 and 1.032 $\pm$ 0.847 g·cm^{-2}. To quantify the contribution of different inputs to the deviation, a stepwise regression was conducted with the LST deviation as the dependent variable and the deviations of ε_{11}, ε_{12}, and w as independent variables. For the second swath, we found that the deviations of the three input parameters explain 31.9% of the LST deviation, the fractions of which that were contributed from the deviations of ε_{11}, ε_{12}, and w were 39.1%, 6.1%, and 54.7%, respectively. However, for the second swath, only 2.3% of the LST deviation can be explained by the three inputs; their contributions are 65.4%, 4.3%, and 30.3%. Therefore, for the two selected granules, the deviation between the GLASS and M*D11_L2 LSTs arises from different input datasets, as well as other sources. Among the inputs, ε_{11} and w have high contributions. Nevertheless, the comparison between the GLASS-MODIS and M*D11_L2 LSTs only demonstrates their close agreement, instead of the actual reliability of GLASS-MODIS LST due to the unknown reliability of M*D11_L2 LST in many regions [25].

IV. SUMMARY AND FUTURE PROSPECTS

GLASS has generated global instantaneous LST products for 1983, 1993, 2003, and 2013 from historical NOAA-7 and NOAA-14 AVHRR data and Terra/Aqua MODIS data. The spatial resolution of the GLASS LST product is 0.05° for 1983 and 1993 and is 1 km for 2003 and 2013. In contrast to other satellite LST products, the algorithm associated with the GLASS LST is a multialgorithm ensemble approach, which is based on nine SWAs selected from 17 initial candidate SWAs that were trained globally. One of the most important advantages of the combination of nine SWAs is that the ensemble estimation is stable in case one SWA has relatively lower accuracy. This algorithm can be easily extended to other polar orbiting and geostationary satellite data.

The algorithm for the GLASS LST product was first tested with global simulation datasets. We found that the multialgorithm ensemble approach yields an accuracy better than 1.0 K when LSEs yield uncertainties of –0.02 to 0.02 and CWVC yields an uncertainty of –1.0 to 1.0 g·cm^{-2}; the accuracy is better than 1.5 K when the uncertainties of LSEs increase to –0.04 to 0.04. Thus, the algorithm can theoretically satisfy the target accuracy of the GLASS LST product, namely, 2.0 K for MODIS LST and 3.0 K for AVHRR LST.

Validation of GLASS LST product is currently in its preliminary stage, and some preliminary results have been obtained. For the GLASS-AVHRR LST, its accuracy is 2.89 K when validated against the measurements from BSRN. Nevertheless, due to the lack of historical, *in situ* measured LST values, the GLASS-AVHRR LST still requires more in-depth comparison or alternative validation strategies to better understand its quality and applicability. For the GLASS-MODIS LST, a validation based on the measurements from six grassland/cropland SURFRAD sites indicates that the mean RMSE values are 1.82–2.15 K at nighttime for Terra/Aqua MODIS in 2003 and 2013; this accuracy is similar to the official MODIS LST product. Validation at an arid shrubland site (i.e., Desert Rock, NV) of SURFRAD shows that the GLASS-MODIS LST yields a systematic underestimation of LST, as does the official MODIS product, due to large variations in surface spectral emissivity. Further comparison confirms the agreement between the GLASS-MODIS LST and official MODIS LST, with MBD/RMSD of –1.19 K/1.87 K and 1.89 K/2.27 K for the two granules under examination.

GLASS LST products can support the long-term analysis of climate change and environmental application. Since the same approach in LST retrieval has been employed for GLASS-AVHRR and GLASS-MODIS LST products, the bias induced by differences in source algorithms can be avoided. Nevertheless, more in-depth validation, comparison, and tests of the GLASS-AVHRR and GLASS-MODIS LST products are still needed. Furthermore, a hybrid approach that is mainly based on the NDVI threshold is employed to determine the LSEs. However, this approach has limitations over arid or sparsely vegetated surfaces and in addressing the dynamics of land surfaces; thus, the quality of the generated LST product may be deteriorated. Therefore, future work will be concentrated on refining this approach. In addition, the orbit drift correction of NOAA AVHRR is an ongoing work intended to generate a long-term, consistent LST product.

REFERENCES

[1] L. Zhou, Y. Tian, S. B. Roy, C. Thorncroft, L. F. Bosart, and Y. Hu, "Impacts of wind farms on land surface temperature," *Nature Clim. Change*, vol. 2, no. 7, pp. 539–543, Jul. 2012.

[2] L. Ding, J. Zhou, X. Zhang, S. Liu, and R. Cao, "Downscaling of surface air temperature over the Tibetan Plateau based on DEM," *Int. J. Appl. Earth Obs. Geoinf.*, vol. 73, pp. 136–147, Dec. 2018.

[3] C. J. Tomlinson, L. Chapman, J. E. Thornes, and C. Baker, "Remote sensing land surface temperature for meteorology and climatology: A review," *Meteorol. Appl.*, vol. 18, pp. 296–306, 2011.

[4] J. D. Kalma, T. R. McVicar, and M. F. McCabe, "Estimating land surface evaporation: A review of methods using remotely sensed surface temperature data," *Surv. Geophys.*, vol. 29, nos. 4–5, pp. 421–469, Oct. 2008.

[5] J. A. Voogt and T. R. Oke, "Thermal remote sensing of urban climates," *Remote Sens. Environ.*, vol. 86, pp. 370–384, 2003.

[6] T. R. H. Holmes, W. T. Crow, C. Hain, M. C. Anderson, and W. P. Kustas, "Diurnal temperature cycle as observed by thermal infrared and microwave radiometers," *Remote Sens. Environ.*, vol. 158, pp. 110–125, 2015.

[7] J. Zhou et al., "A thermal sampling depth correction method for land surface temperature estimation from satellite passive microwave observation over barren land," *IEEE Trans. Geosci. Remote Sens.*, vol. 55, no. 8, pp. 4743–4756, Aug. 2017.

[8] J. Zhou, F. Dai, X. Zhang, S. Zhao, and M. Li, "Developing a temporally land cover-based look-up table (TL-LUT) method for estimating land surface temperature based on AMSR-E data over the Chinese landmass," *Int. J. Appl. Earth Obs. Geoinf.*, vol. 34, pp. 35–50, 2015.

[9] S.-B. Duan, Z.-L. Li, and P. Leng, "A framework for the retrieval of all-weather land surface temperature at a high spatial resolution from polar-orbiting thermal infrared and passive microwave data," *Remote Sens. Environ.*, vol. 195, pp. 107–117, Jun. 2017.

[10] Z.-L. Li et al., "Satellite-derived land surface temperature: Current status and perspectives," *Remote Sens. Environ.*, vol. 131, pp. 14–37, 2013.

[11] F. Becker and Z.-L. Li, "Towards a local split window method over land surfaces," *Int. J. Remote Sens.*, vol. 11, pp. 369–393, Mar. 1990.

[12] Z. Wan and J. Dozier, "A generalized split-window algorithm for retrieving land-surface temperature from space," *IEEE Trans. Geosci. Remote Sens.*, vol. 34, no. 4, pp. 892–905, Jul. 1996.

[13] Z. Qin, A. Karnieli, and P. Berliner, "A mono-window algorithm for retrieving land surface temperature from Landsat TM data and its application to the Israel-Egypt border region," *Int. J. Remote Sens.*, vol. 22, pp. 3719–3746, Jan. 2001.

[14] J. C. Jiménez-Muñoz and J. A. Sobrino, "A generalized single-channel method for retrieving land surface temperature from remote sensing data," *J. Geophys. Res. Atmos.*, vol. 108, pp. 4688–4695, 2003.

[15] A. Gillespie, S. Rokugawa, T. Matsunaga, J. S. Cothern, S. Hook, and A. B. Kahle, "A temperature and emissivity separation algorithm for Advanced Spaceborne Thermal Emission and Reflection Radiometer (ASTER) images," *IEEE Trans. Geosci. Remote Sens.*, vol. 36, no. 4, pp. 1113–1126, Jul. 1998.

[16] G. C. Hulley and S. J. Hook, "Generating consistent land surface temperature and emissivity products between ASTER and MODIS data for earth science research," *IEEE Trans. Geosci. Remote Sens.*, vol. 49, no. 4, pp. 1304–1315, Apr. 2011.

[17] J. C. Jiménez-Muñoz, J. A. Sobrino, C. Mattar, G. Hulley, and F. M. Gottsche, "Temperature and emissivity separation from MSG/SEVIRI data," *IEEE Trans. Geosci. Remote Sens.*, vol. 52, no. 9, pp. 5937–5951, Sep. 2014.

[18] S. Liang, "An optimization algorithm for separating land surface temperature and emissivity from multispectral thermal infrared imagery," *IEEE Trans. Geosci. Remote Sens.*, vol. 39, no. 2, pp. 264–274, Feb. 2001.

[19] Z. Wan and Z.-L. Li, "A physics-based algorithm for retrieving land-surface emissivity and temperature from EOS/MODIS data," *IEEE Trans. Geosci. Remote Sens.*, vol. 35, no. 4, pp. 980–996, Jul. 1997.

[20] C. Coll, V. García-Santos, R. Niclòs, and V. Caselles, "Test of the MODIS land surface temperature and emissivity separation algorithm with ground measurements over a rice paddy," *IEEE Trans. Geosci. Remote Sens.*, vol. 54, no. 5, pp. 3061–3069, May 2016.

[21] Z. Wan, "New refinements and validation of the collection-6 MODIS land-surface temperature/emissivity product," *Remote Sens. Environ.*, vol. 140, pp. 36–45, 2014.

[22] Z. Wan, "New refinements and validation of the MODIS land-surface temperature/emissivity products," *Remote Sens. Environ.*, vol. 112, no. 1, pp. 59–74, Jan. 2008.

[23] D. Sun, "Estimation of land surface temperature from a Geostationary Operational Environmental Satellite (GOES-8)," *J. Geophys. Res.*, vol. 108, no. D11, 2003, Art. no. 4326.

[24] Y. Yu, J. L. Privette, and A. C. Pinheiro, "Analysis of the NPOESS VIIRS land surface temperature algorithm using MODIS data," *IEEE Trans. Geosci. Remote Sens.*, vol. 43, no. 10, pp. 2340–2350, Oct. 2005.

[25] P. C. Guillevic et al., "Validation of land surface temperature products derived from the Visible Infrared Imaging Radiometer Suite (VIIRS) using ground-based and heritage satellite measurements," *Remote Sens. Environ.*, vol. 154, pp. 19–37, 2014.

[26] F. Prata, "Land surface temperature measurement from space: AATSR algorithm theoretical basis," CSIRO Atmospheric Research, Aspendale, Vic., Australia, Contract report to ESA, 2002.

[27] D. J. Ghent, G. K. Corlett, F.-M. Göttsche, and J. J. Remedios, "Global land surface temperature from the along-track scanning radiometers," *J. Geophys. Res. Atmos.*, vol. 122, no. 22, pp. 12167–12193, Nov. 2017.

[28] L. Dong, H. Yang, P. Zhang, S. Tang, and Q. Lu, "Retrieval of land surface temperature and dynamic monitoring of a high temperature weather process based on FY-3A/VIRR data," *J. Appl. Meteorol. Sci.*, vol. 23, no. 2, pp. 214–221, 2012.

[29] I. F. Trigo, I. T. Monteiro, F. Olesen, and E. Kabsch, "An assessment of remotely sensed land surface temperature," *J. Geophys. Res. Atmos.*, vol. 113, 2008, Art. no. D17108.

[30] S. C. Freitas, I. F. Trigo, J. M. Bioucas-Dias, and F. M. Göttsche, "Quantifying the uncertainty of land surface temperature retrievals from SEVIRI/Meteosat," *IEEE Trans. Geosci. Remote Sens.*, vol. 48, no. 1, pp. 523–534, Jan. 2010.

[31] F.-M. Göttsche, F.-S. Olesen, I. F. Trigo, A. Bork-Unkelbach, and M. A. Martin, "Long term validation of land surface temperature retrieved from MSG/SEVIRI with continuous in-situ measurements in Africa," *Remote Sens.*, vol. 8, no. 5, May 2016, Art. no. 410.

[32] S. L. Ermida, I. F. Trigo, C. C. DaCamara, F. M. Göttsche, F. S. Olesen, and G. Hulley, "Validation of remotely sensed surface temperature over an oak woodland landscape—The problem of viewing and illumination geometries," *Remote Sens. Environ.*, vol. 148, pp. 16–27, 2014.

[33] L. Fang, Y. Yu, H. Xu, and D. Sun, "New retrieval algorithm for deriving land surface temperature from geostationary orbiting satellite observations," *IEEE Trans. Geosci. Remote Sens.*, vol. 52, no. 2, pp. 819–828, Feb. 2014.

[34] J. Zhou, Y. Chen, X. Zhang, and W. Zhan, "Modelling the diurnal variations of urban heat islands with multi-source satellite data," *Int. J. Remote Sens.*, vol. 34, no. 21, pp. 7568–7588, Nov. 2013.

[35] Y. Yamamoto, H. Ishikawa, Y. Oku, and Z. Hu, "An algorithm for land surface temperature retrieval using three thermal infrared bands of Himawari-8," *J. Meteorol. Soc. Jpn. Ser. II*, vol. 96B, pp. 59–76, 2018.

[36] S. C. Freitas, I. F. Trigo, J. Macedo, C. Barroso, R. Silva, and R. Perdigão, "Land surface temperature from multiple geostationary satellites," *Int. J. Remote Sens.*, vol. 34, nos. 9–10, pp. 3051–3068, May 2013.

[37] E. E. Borbas, S. W. Seemann, H. L. Huang, J. Li, and W. P. Menzel, "Global profile training database for satellite regression retrievals with estimates of skin temperature and emissivity," in *Proc. XIV Int. ATOVS Study Conf.*, Beijing, China, 2005, pp. 763–770.

[38] J. Zhou, Y. Wang, J. Cheng, S. Liang, F. Huang, and F. Dai, "GLASS - Global land surface temperature product: Algorithm theoretical basis document (version 1.0)," Beijing Normal Univ., Beijing, China, 2016.

[39] A. Berk et al., "MODTRAN 5: A reformulated atmospheric band model with auxiliary species and practical multiple scattering options: Update," *Proc. SPIE*, vol. 5806, pp. 662–667, 2005.

[40] A. M. Baldridge, S. J. Hook, C. I. Grove, and G. Rivera, "The ASTER spectral library version 2.0," *Remote Sens. Environ.*, vol. 113, no. 4, pp. 711–715, Apr. 2009.

[41] F. Huang, J. Zhou, J. Tao, X. Tan, S. Liang, and J. Cheng, "PMODTRAN: A parallel implementation based on MODTRAN for massive remote sensing data processing," *Int. J. Digit. Earth*, vol. 9, no. 9, pp. 819–834, Sep. 2016.

[42] M. Hansen, R. DeFries, J. R. G. Townshend, and R. Sohlberg, "UMD global land cover classification, 1 kilometer, 1.0 (1981-1994)," Dept. Geography, Univ. Maryland, College Park, MD, USA, 1998.

[43] Y. Yu, J. L. Privette, and A. C. Pinheiro, "Evaluation of split-window land surface temperature algorithms for generating climate data records," *IEEE Trans. Geosci. Remote Sens.*, vol. 46, no. 1, pp. 179–192, Jan. 2008.

[44] J. Zhou, X. Zhang, W. Zhan, and H. Zhang, "Land surface temperature retrieval from MODIS data by integrating regression models and the genetic algorithm in an arid region," *Remote Sens.*, vol. 6, no. 6, pp. 5344–5367, Jun. 2014.

[45] C. Ottlé and D. Vidal-Madjar, "Estimation of land surface temperature with NOAA9 data," *Remote Sens. Environ.*, vol. 40, pp. 27–41, 1992.

[46] C. Francois and C. Ottle, "Atmospheric corrections in the thermal infrared: Global and water vapor dependent split-window algorithms-applications to ATSR and AVHRR data," *IEEE Trans. Geosci. Remote Sens.*, vol. 34, no. 2, pp. 457–470, Mar. 1996.

[47] J. C. Price, "Land surface temperature measurements from the split window channels of the NOAA 7 Advanced Very High Resolution Radiometer," *J. Geophys. Res. Atmos.*, vol. 89, pp. 7231–7237, 1984.

[48] C. Ulivieri and G. Cannizzaro, "Land surface temperature retrievals from satellite measurements," *Acta Astronaut.*, vol. 12, no. 12, pp. 977–985, 1985.

[49] A. J. Prata and C. M. R. Platt, "Land surface temperature measurements from the AVHRR," in *Proc. 5th AVHRR Data Users Conf.*, Tromso, Norway, 1991, pp. 433–438.

[50] A. Vidal, "Atmospheric and emissivity correction of land surface temperature measured from satellite using ground measurements or satellite data," *Int. J. Remote Sens.*, vol. 12, pp. 2449–2460, Dec. 1991.

[51] C. Ulivieri, M. M. Castronuovo, R. Francioni, and A. Cardillo, "A split window algorithm for estimating land surface temperature from satellites," *Adv. Space Res.*, vol. 14, pp. 59–65, 1994.

[52] J. Sobrino, C. Coll, and V. Caselles, "Atmospheric correction for land surface temperature using NOAA-11 AVHRR channels 4 and 5," *Remote Sens. Environ.*, vol. 38, pp. 19–34, 1991.

[53] C. Coll, V. Caselles, J. A. Sobrino, and E. Valor, "On the atmospheric dependence of the split-window equation for land surface temperature," *Int. J. Remote Sens.*, vol. 15, pp. 105–122, Jan. 1994.

[54] J. A. Sobrino and N. Raissouni, "Toward remote sensing methods for land cover dynamic monitoring: Application to Morocco," *Int. J. Remote Sens.*, vol. 21, pp. 353–366, Jan. 2000.

[55] Y. Ma and O. Tsukamoto, *Combining Satellite Remote Sensing With Field Observations for Land Surface Heat Fluxes Over Inhomogeneous Landscape*. Beijing, China: China Meteorol. Press, 2002.

[56] F. Becker and Z.-L. Li, "Surface temperature and emissivity at various scales: Definition, measurement and related problems," *Remote Sens. Rev.*, vol. 12, pp. 225–253, Jan. 1995.

[57] J. M. Galve, C. Coll, V. Caselles, and E. Valor, "An atmospheric radiosounding database for generating land surface temperature algorithms," *IEEE Trans. Geosci. Remote Sens.*, vol. 46, no. 5, pp. 1547–1557, May 2008.

[58] J. A. Sobrino, N. Raissouni, and Z.-L. Li, "A comparative study of land surface emissivity retrieval from NOAA data," *Remote Sens. Environ.*, vol. 75, pp. 256–266, 2001.

[59] M. M. Rienecker *et al.*, "MERRA: NASA's modern-era retrospective analysis for research and applications," *J. Clim.*, vol. 24, pp. 3624–3648, Jul. 2011.

[60] A. Chedin, N. A. Scott, C. Wahiche, and P. Moulinier, "The improved initialization inversion method: A high resolution physical method for temperature retrievals from satellites of the TIROS-N series," *J. Clim. Appl. Meteorol.*, vol. 24, pp. 128–143, Feb. 1985.

[61] F. Chevallier, F. Chéruy, N. A. Scott, and A. Chédin, "A neural network approach for a fast and accurate computation of a longwave radiative budget," *J. Appl. Meteorol.*, vol. 37, pp. 1385–1397, Nov. 1998.

[62] H. Wu, X. Zhang, S. Liang, H. Yang, and G. Zhou, "Estimation of clear-sky land surface longwave radiation from MODIS data products by merging multiple models," *J. Geophys. Res. Atmos.*, vol. 117, 2012, Art. no. D22107.

[63] Y. Yao *et al.*, "Bayesian multimodel estimation of global terrestrial latent heat flux from eddy covariance, meteorological, and satellite observations," *J. Geophys. Res. Atmos.*, vol. 119, pp. 4521–4545, 2014.

[64] Q. Duan and T. J. Phillips, "Bayesian estimation of local signal and noise in multimodel simulations of climate change," *J. Geophys. Res. Atmos.*, vol. 115, 2010, Art. no. D18123.

[65] A. C. T. Pinheiro, R. Mahoney, J. L. Privette, and C. J. Tucker, "Development of a daily long term record of NOAA-14 AVHRR land surface temperature over Africa," *Remote Sens. Environ.*, vol. 103, pp. 153–164, 2006.

[66] J. A. Sobrino *et al.*, "Land surface emissivity retrieval from different VNIR and TIR sensors," *IEEE Trans. Geosci. Remote Sens.*, vol. 46, no. 2, pp. 316–327, Feb. 2008.

[67] J. Zhou, M. Li, S. Liu, Z. Jia, and Y. Ma, "Validation and performance evaluations of methods for estimating land surface temperatures from ASTER data in the middle reach of the Heihe River basin, northwest China," *Remote Sens.*, vol. 7, no. 6, pp. 7126–7156, May 2015.

[68] K. Wang and S. Liang, "Evaluation of ASTER and MODIS land surface temperature and emissivity products using long-term surface longwave radiation observations at SURFRAD sites," *Remote Sens. Environ.*, vol. 113, pp. 1556–1565, 2009.

[69] Y. Yi, J. Kimball, L. A. Jones, R. H. Reichle, and K. Mcdonald, "Evaluation of MERRA land surface estimates in preparation for the soil moisture active passive mission," *J. Clim.*, vol. 24, pp. 3797–3816, Aug. 2011.

Ji Zhou (M'11) received the B.S. degree in geographic information system from Nanjing University, Nanjing, China, in 2005, and the Ph.D. degree in geography from Beijing Normal University, Beijing, China, in 2010.

He was a visiting Ph.D. student at the Department of Geography, University of Western Ontario, London, ON, Canada, from 2008 to 2009. From 2015 to 2016, he was an International Research Fellow with the European Space Agency, Rome, Italy. He is currently a Professor with the School of Resources and Environment and Center for Information Geoscience, University of Electronic Science and Technology of China, Chengdu, China. His research interest focuses on thermal and passive microwave remote sensing of land surfaces.

Shunlin Liang (M'94–F'13) received the Ph.D. degree from Boston University, Boston, MA, USA, in 1993.

He is currently a Professor with the Department of Geographical Sciences, University of Maryland, College Park, MD, USA. He has authored or co-authored more than 320 SCI indexed peer-reviewed journal papers and 32 book chapters. He authored/edited six books and four of which were also published in Chinese, such as *Quantitative Remote Sensing of Land Surfaces* (Wiley, 2004), *Advances in Land Remote Sensing: System, Modeling, Inversion and Application* (Springer, 2008), *Advanced Remote Sensing: Terrestrial Information Extraction and Applications* (Academic Press, 2012), *Global Land Surface Satellite (GLASS) Products: Algorithms, Validation and Analysis* (Springer, 2013), *Land Surface Observation, Modeling, Data Assimilation* (World Scientific, 2013), and *Earth's Energy Budget* (Elsevier, 2017). He was the Editor-in-Chief of the nine-volume books entitled *Comprehensive Remote Sensing* (Elsevier, 2017). His main research interests include estimation of land surface variables from satellite data, Earth's energy balance, and assessment of environmental changes.

Dr. Liang was an Associate Editor for the IEEE TRANSACTION ON GEO-SCIENCE AND REMOTE SENSING and also a Guest Editor for several remote sensing related journals.

Jie Cheng (M'11) received the Ph.D. degree in cartography and remote sensing from the Institute of Remote Sensing Applications of Chinese Academy of Sciences, Beijing, China, in 2008.

He was a Postdoctoral Fellow with the State Key Laboratory of Remote Sensing Science, Beijing Normal University, Beijing, China, from 2008 to 2010, and an Assistant Research Scientist with the University of Maryland, College Park, from 2009 to 2010. He is currently an Associate Professor with the State Key Laboratory of Remote Sensing Science, Faculty of Geography, Beijing Normal University, and a Visiting Scientist with the Hydrology and Remote Sensing Laboratory, United States Department of Agriculture-Agricultural Research Service, Beltsville, MD, USA. His main research interests include estimation of land surface variables from satellite observations, radiative transfer modeling, and studies on surface energy balance.

Yujia Wang, photograph and biography are not available at the time of publication.

Jin Ma (S'16) received the B.S. degree in geographic information system from Chengdu University of Technology, Chengdu, China, in 2015. He is currently working toward the Ph.D. degree in remote sensing at the School of Resources and Environment and Center for Information Geoscience, University of Electronic Science and Technology of China, Chengdu, China.

His research interest focuses on thermal remote sensing of land surface temperature and its validation.